Journal of Hazardous Materials 497 (2025) 139646

Contents lists available at ScienceDirect

Journal of Hazardous Materials

journal homepage: www.elsevier.com/locate/jhazmat

Deciphering uptake mechanisms of potentially toxic elements in seaweeds using high resolution imaging analysis

Antón Vázquez-Arias [a,*], Conxi Rodríguez-Prieto [b], Yosuke Yamada [c,d], Motoo Ito [c], J. Ángel Fernández [e], Jesús R. Aboal [e]

[a] Bioaplic Research Group, Department of Botany, Faculty of Biology, Universidade de Santiago de Compostela, Santiago de Compostela 15782, Spain
[b] Department of Environmental Sciences, Faculty of Sciences, Universitat de Girona, Girona 17003, Spain
[c] Kochi Institute for Core Sample Research, Japan Agency for Marine-Earth Science and Technology (JAMSTEC), Nankoku, Kochi, Japan
[d] Advanced Institute for Marine Ecosystem Change (WPI-AIMEC), JAMSTEC, Yokohama, Kanagawa, Japan
[e] CRETUS Institute, Ecology Area, Department of Functional Biology, Faculty of Biology, Universidade de Santiago de Compostela, Santiago de Compostela 15782, Spain

HIGHLIGHTS

- Pb is retained in the cell wall, with negligible intracellular accumulation.
- Zn and Mn are internalized and stored in organelles like physodes and plastids.
- Pb concentrations depend on environmental availability.
- Concentrations of intracellular PTEs are metabolically regulated.

GRAPHICAL ABSTRACT

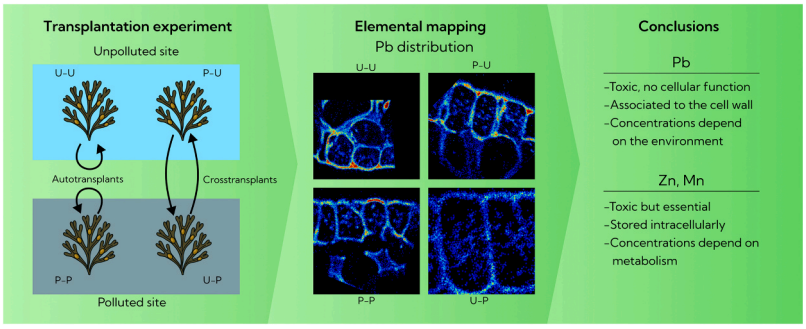

ARTICLE INFO

Keywords:
Marine pollution
Heavy metals
PTEs
Macroalgae
Fucus vesiculosus

ABSTRACT

Pollution by potentially toxic elements (PTEs) such as Pb and Zn threatens seaweed populations, which sustain marine coastal ecosystems. Understanding how seaweeds uptake and release these pollutants is crucial to assessing their impact. To address this, we analyzed the subcellular location of PTEs in transplanted thalli of the brown seaweed *Fucus vesiculosus* using nanoscale secondary ion mass spectrometry (NanoSIMS). Lead accumulated primarily in the cell wall, with minimal intracellular localization. Its concentrations increased slightly upon exposure at a polluted site and decreased at an unpolluted site, reflecting an equilibrium between environmental bioavailability and cell wall binding sites. In contrast, metabolically important PTEs such as Mn and Zn exhibited higher intracellular concentrations that responded similarly when transplanted to a different site regardless of its pollution levels, likely as a stress response to changes in environmental conditions. PTEs without metabolic functions, such as Pb, are not internalized and remain in equilibrium with the environment, whereas intracellular essential PTEs are metabolically regulated. This contrast explains why PTEs differ in toxicity to seaweeds, advancing our understanding of their vulnerability to pollution and enabling more effective strategies to protect the ecosystems they support.

* Corresponding author.
E-mail address: antonvazquez.arias@usc.es (A. Vázquez-Arias).

https://doi.org/10.1016/j.jhazmat.2025.139646
Received 20 May 2025; Received in revised form 2 August 2025; Accepted 22 August 2025
Available online 23 August 2025

1. Introduction

Coastal ecosystems are essential for marine life and human communities, as they sustain rich biodiversity, support key activities, and supply vital resources [27,9]. Yet, these ecosystems are among the most vulnerable to anthropogenic impact, hosting numerous industrial, transportation and recreational activities, while also receiving discharges from rivers, which are often used for waste disposal [21]. This has led to the accumulation of pollutants in coastal areas, causing significant environmental degradation and disrupting marine ecosystems.

Among the most harmful pollutants in coastal waters are potentially toxic elements (PTEs). For instance, the use of Cu and Zn in antifouling paints has resulted in severe contamination of harbor waters [16,4]; discharges from rivers affected by acid mine drainage containing Cu, As, and other PTEs, have damaged ecosystems around river mouths [18,20,3]; and concentrations of Pb and Hg in marine environments have increased tenfold compared to preindustrial levels [11,23].

In these environments, seaweeds are foundational organisms, providing food, physical structure, cycling nutrients, and sequestering carbon, thereby supporting biodiversity and ecosystem resilience [24,31]. Understanding their interactions with PTEs is therefore essential for assessing and predicting the impact of pollution on the ecosystems they sustain. Additionally, seaweeds are commonly used in biomonitoring studies to assess pollution in coastal ecosystems [12,13], with the accuracy of these assessments relying on our understanding of seaweed-PTE interactions. Still, until recently, little was known about the pathways and fate of the PTEs captured by seaweeds [36].

Over the last two decades, two techniques have emerged that enable the imaging of elemental concentrations with the sensitivity required to map natural distributions of PTEs at the nanoscale, driving significant progress in this field [7]. These techniques are synchrotron-based X-Ray diffraction (S-XRF) and nanoscale secondary ion mass spectrometry (NanoSIMS), both of which allow mapping elemental concentrations at resolutions as low as tens of nanometers [39]. These technologies operate on different principles: S-XRF uses an X-ray beam to excite the atoms in the sample and analyzes the resulting fluorescence emission spectrum, while NanoSIMS employs an ion beam to scatter secondary ions from the sample, which are then analyzed by mass spectrometry. These different principles lead to distinct advantages and limitations. S-XRF provides data on a wide range of elements within a single spectrum, but is primarily limited to heavy elements and overlap between fluorescence peaks can cause interferences in the analysis of fixed samples. With NanoSIMS, the number of elements analyzed simultaneously is lower, but it can also be used to detect light elements that are beyond the reach of S-XRF [39] and is able to provide higher resolution [19].

To date, very few studies have applied these techniques to seaweed. NanoSIMS studies have focused exclusively on *Laminaria digitata*, a kelp species, analyzing the distribution of As, Br, and I—all of which were found to accumulate extracellularly [10,17,37]. Similarly, S-XRF analysis conducted on *Laminaria digitata* detected Sr outside the cells, while Fe and Zn were colocalized intracellularly. Most of the information available on PTEs distributions at nanoscale comes from a study on the fucoid *Fucus vesiculosus*, which revealed two distinct accumulation patterns for PTEs [35]. Elements without significant metabolic roles (e.g., As, Ba, and U) were found to accumulate extracellularly, whereas metabolically essential PTEs (e.g., Co, Ni, Cu, and Zn) were internalized and sequestered into physodes—specialized organelles containing phenolic compounds known as phlorotannins. Although these studies provide a strong foundation for understanding PTE uptake in seaweeds, mainly two important questions remain unanswered. First, although the metabolic role of elements has been suggested to influence their accumulation patterns, key PTEs without metabolic functions (e.g. Pb, Cd, and Hg) were undetectable in previous S-XRF studies. Second, while some inferences about accumulation mechanisms and dynamics can be drawn from existing data—for example, elements attached to the cell wall are likely bound by ionic interactions—the dynamics and mechanisms controlling intracellular concentrations remain poorly understood. Key uncertainties include the rate of the internalization process, its reversibility, and the molecular mechanisms governing membrane transport. Addressing these gaps would enhance our understanding of PTE toxicity under varying environmental conditions and the potential for its reduction by reducing environmental PTE concentrations.

In this study, we aim to address both limitations. We conducted a transplantation experiment between two sites with differing pollution levels to investigate the cellular structures responsible for capturing and discharging PTEs in response to changes in environmental concentrations. The samples were analyzed using NanoSIMS, which enabled us to resolve the distribution of Pb, which was undetectable in previous S-XRF studies, among other PTEs.

2. Material and methods

2.1. Transplant preparation and exposure

A transplantation experiment was conducted between two nearby exposure sites (ES) in NW Spain characterized by different pollution levels. The first site, located at 42°47'25.3"N, 8°55'04.1"W (WGS84) has overall low PTE concentrations, whereas the second site, located at 42°20'46.7"N, 8°36'47.9"W, has high Pb concentrations owing to a nearby inactive porcelain factory. Because Pb was the main focus of this study, the polluted site was selected for its extreme Pb concentrations in seaweeds and sediments [33]. However, the concentrations of other elements are not particularly high at this site, as shown in a previous transplantation study [34], in which transplants taken from the unpolluted to the polluted site experienced a decrease in Mn concentrations, and Zn concentrations remained mostly stable. Still, contrasting concentrations for most elements between the two locations enable testing our hypothesis.

Thalli of *Fucus vesiculosus* and two stones roughly 20 × 20 x 10 cm in size were collected from each site. Transplants mimicking natural conditions were prepared by attaching four medium-sized thalli to each stone: two stones were prepared with thalli from the polluted site, and two with thalli from the unpolluted site. The thalli were secured to the upper surface of the stones using waterproof silicone sealant. To prevent material loss while allowing water flow, the stones were covered with 2 cm mesh size polyethylene nets. The prepared transplants were left at 4°C overnight. The following day, one transplant from each site was placed at each ES, ensuring that each site contained one transplant with local seaweed (autotransplant) and one with seaweed from the opposite site (cross-transplant). To avoid confusion, the following codes will be used in the text and figures: autotransplants in the unpolluted site (U-U), autotransplants in the polluted site (P-P), cross-transplants from unpolluted to polluted (U-P), and cross-transplants from polluted to unpolluted (P-U).

The transplants were collected after 12 days, a timeframe shown to be sufficient for detecting changes in PTE concentrations in seaweeds exposed to different conditions [36]. The dismantling process involved mesh nets and scraping off the silicone sealant. The thalli were collected and placed in polyethylene bags for transport to the laboratory. To ensure homogeneity, the three apical dichotomies of healthy thalli without reproductive structures were selected. Two apices from each of the four samples were further selected for SEM and NanoSIMS analysis. These apices were stored in polypropylene tubes containing a small amount of water to prevent dehydration, and kept at 4°C. The remaining material was oven-dried at 40°C until constant weight, homogenized with a tangential mill with zirconium oxide grinding vessels (Retsch ZM400), and stored in darkness until chemical analysis.

2.2. ICP-MS analysis

The samples were oven-dried at 40 ºC to remove residual moisture

before analysis. From each sample, 1 g (dry weight) was digested in Teflon vessels using a microwave digestion system (Milestone Ethos-1) following a temperature ramp: 100 ºC for 10 min, 150 ºC for 7 min, and 190 ºC for 25 min. The digestion was performed with 10 mL of HNO_3 (65 %), 2 mL of H_2O_2 (30 %), and 2 mL of Milli-Q water. Total concentrations of Na, Ca, Mn, Zn, and Pb were determined by inductively coupled plasma mass spectrometry (ICP-MS, Agilent 7700x) at the University Research Support Services Unit (RIAIDT, Universidade de Santiago de Compostela). Quality control was ensured through replicate analyses and the use of reference material (ERM-CD200, *Fucus vesiculosus*). The variation among replicates ranged from 9 % to 11 % and the percentage recoveries for the two certified elements—Zn and Pb—were 113 % and 96 % respectively.

2.3. Sample preparation for scanning electron microscope (SEM) and NanoSIMS

Within 24 h of collection, the samples in polypropylene tubes were transported under refrigeration to the Centro Nacional de Biotecnología (CNB-CSIC) in Madrid, Spain, for preparation for SEM and NanoSIMS analysis. The samples were prepared by cryofixation to prevent the mobilization of trace elements [37]. The fixation protocol is described in Vázquez-Arias et al. [35]. Briefly, 150 µm-thick transverse sections were subjected to high-pressure freezing, vitrified in a 1 % osmium tetroxide solution in acetone, and dehydrated with anhydrous acetone. Finally, the samples were embedded in epoxy resin. All 4 samples had well-preserved regions suitable for analyses.

From each resin block, 200 nm-thick sections were obtained and transferred onto 5 × 5 mm silicon wafers. The sections were stained with saturated aqueous uranyl acetate for 25 min at room temperature and mounted on SEM aluminum holders using conductive carbon tape.

2.4. SEM imaging

The mounted samples were transported to the Research Support Services Unit of the University of Santiago de Compostela (RIAIDT-USC) for SEM analysis. Images were captured to visualize the samples and identify the best-preserved regions for NanoSIMS analysis. Low-resolution exploratory images were obtained using a Zeiss EVO 15, while high-resolution close-up images were captured with a Zeiss Gemini 500. The cellular ultrastructure was visualized using backscatter detectors.

2.5. NanoSIMS analysis

The mounted sections were analyzed using a CAMECA NanoSIMS 50 L at the Kochi Institute for Core Sample Research (KOCHI-JAMSTEC) in Japan. Samples were pre-sputtered at high beam currents (~100 pA), and analyzed with a 16 keV primary O^- beam (Hyperion RF source apparatus) at around 7 pA (D1–2, Do-2 conditions). Areas measuring 48 × 48 µm were scanned with an approximate spatial resolution of 200 nm and an acquisition time of 10 ms per pixel, obtaining 256 × 256-pixel images. Each area was analyzed 5 times, taking 3311 s. Positive secondary ion images of ^{23}Na, ^{40}Ca, ^{55}Mn, ^{64}Zn, ^{208}Pb, and $^{238}U^{16}O$ were obtained simultaneously by multidetection with six electron multipliers at a mass resolving power of approximately ~3000 (CAMECA NanoSIMS definition), producing read counts (number of ions acquired) for each pixel. Four samples were analyzed, and in three of them more than one area was measured to compare inter- and intra-sample variability.

As uranyl acetate was used during the staining process, UO maps were generated to assist in visualizing ultrastructural elements and aligning them with SEM images; however, these maps do not reflect natural U distributions. The other five elements where selected for different reasons: Ca and Na are metals detectable with the O^- beam with high concentrations which also assist in structural identification; Zn and Mn are were previously studied in *F. vesiculosus* [35], allowing the validation of the NanoSIMS results; and among key PTEs with unknown distributions seaweeds (Pb, Cd, and Hg), Pb was selected for analysis due to its extreme toxicity and comparatively high environmental concentrations.

2.6. Data processing

Image processing was performed using ImageJ [28] and NASA JSC imaging software [15]. The.im NanoSIMS data files were opened using the OpenMIMS plugin [25], which was used to export them as PNG files for visualization and as TIFFs for statistical analysis. To overlay SEM and NanoSIMS images, an affine transformation was applied to the NanoSIMS images using the Landmark Correspondence tool. For regions where SEM images with at least 2000x magnification and corresponding NanoSIMS data available, intensity values of the different elements in the ultrastructural components of the samples were extracted. This level of magnification was necessary to accurately identify small organelles. For each of the four samples, this analysis was conducted in two regions, except for the worst preserved sample, where only one region could be analyzed. Ultrastructural elements were selected as regions of interest (ROIs) on the SEM images, which were then applied to the TIFF files to retrieve element intensity values across pixels within the ROIs. Cellular structures were identified following previous studies [35]. The main structures identified were the cell wall, nuclei, plastids, vacuoles, mitochondria, and physodes. Extracellular polysaccharides were also identified but were grouped with the cell wall due to their similar composition. Cytoplasmic regions were excluded from analysis as they could not be consistently identified across all samples due to tightly packed vacuoles and limited contrast. Most analyses focused on regions close to the surface (meristoderm and cortex), as these cellular layers are primarily responsible for PTE accumulation [35].

2.7. Data analysis

The extracted data were analyzed using R software version 4.4.1 (R [26]), with data visualization performed using the ggplot2 [38] package. The median concentration for each subcellular structure was calculated by aggregating data from all pixels within its ROI across all five layers. The median was used instead of the mean to ensure robustness against pixels from surrounding structures that may have been incorrectly included due to minor errors in image alignment or ROI selection.

The use of statistical tests to compare concentration values was hindered by two factors: slight differences in intensity values introduced by NanoSIMS analysis and the large number of pixel values. As previously reported [35], applying statistical tests to pixel values can inflate statistical power, resulting in low p-values for every comparison. For this reason, techniques such non-parametric statistical tests comparing medians are unable to distinguish biologically meaningful differences from slight biases caused by methodological artifacts such as matrix effects. A possible alternative could be comparing the medians values of subcellular structures, but this is complicated by the differences in abundance. While the large number of physodes allowed for meaningful comparisons, the continuity of the cell wall and the limited number of nuclei restricted such comparisons. Therefore, sample comparisons were performed visually, as the combination of distribution maps and graphs comparing median values enable the description of concentrations distribution patterns. For these comparisons, structures from different cellular layers (meristoderm and cortex) were grouped, as prior studies [35] reported only minor differences in elemental concentrations between these layers.

3. Results

The NanoSIMS concentration maps, SEM images, and their overlays are shown in Figs. 1 and 2 for PTEs in selected samples, with the

remainder presented in Figs. S1–S4 of the supplementary material. Each element exhibited distinct distribution patterns which were generally consistent across different samples. Na showed some variability, with high concentrations in the cell walls of most samples but higher intracellular concentrations in the vacuoles of certain samples. For Ca, the highest concentrations were found in the cell wall, followed by the physodes and plastids. Mn was predominantly detected intracellularly, particularly within the plastids. Zn was primarily concentrated in the physodes, although significant concentrations were also observed in the cell wall of some samples. Pb was mostly concentrated in the cell wall, with minimal intracellular presence; intracellularly, it was restricted to the physodes.

Fig. 3 shows the median concentrations of each element by sample and ultrastructural element, enabling the study of exposure site effects. For all elements except Pb, the cross-transplants (U-P and P-U) experienced similar trends regardless of the exposure site. Specifically, the concentrations of Ca, Mn and Zn were lower in the cross-transplants than in the autotransplants of the same origin, whereas Na concentrations increased in the cross-transplants. These trends were consistent across subcellular structures. Pb, however followed a distinct pattern aligned with expected site-related effects. Samples collected from the unpolluted site had higher Pb concentrations when exposed at the

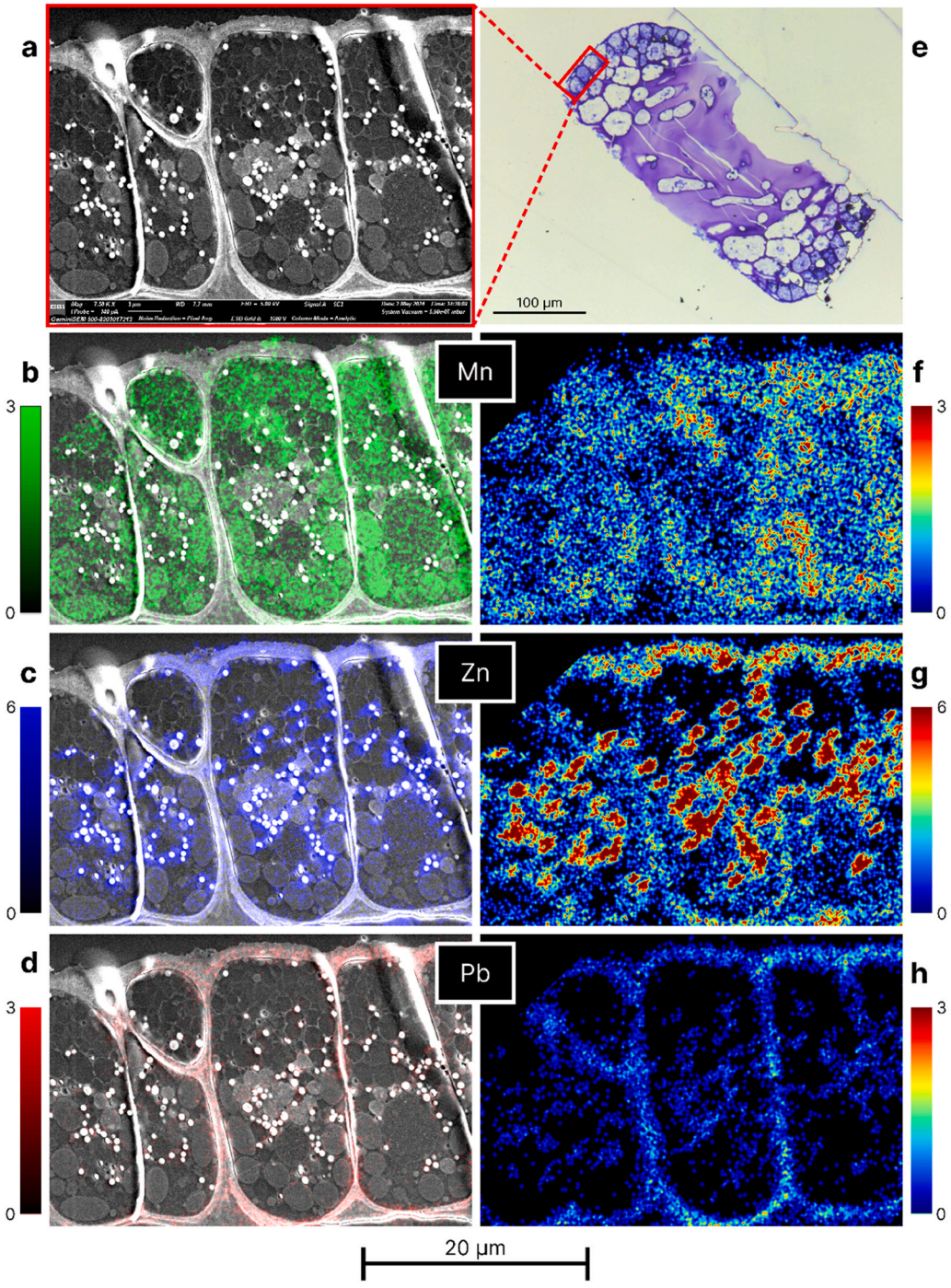

Fig. 1. SEM and NanoSIMS images of the P-U sample. a: SEM image. b-d: Elemental distribution maps of Mn, Zn, and Pb overlayed over the SEM image. e: Optical image of a section from a different *F. vesiculosus* sample stained with toluidine blue. f-h: Distribution maps with a color scale over for enhanced contrast. Color scale units are NanoSIMS read counts. Bottom scale applies to SEM and NanoSIMS images.

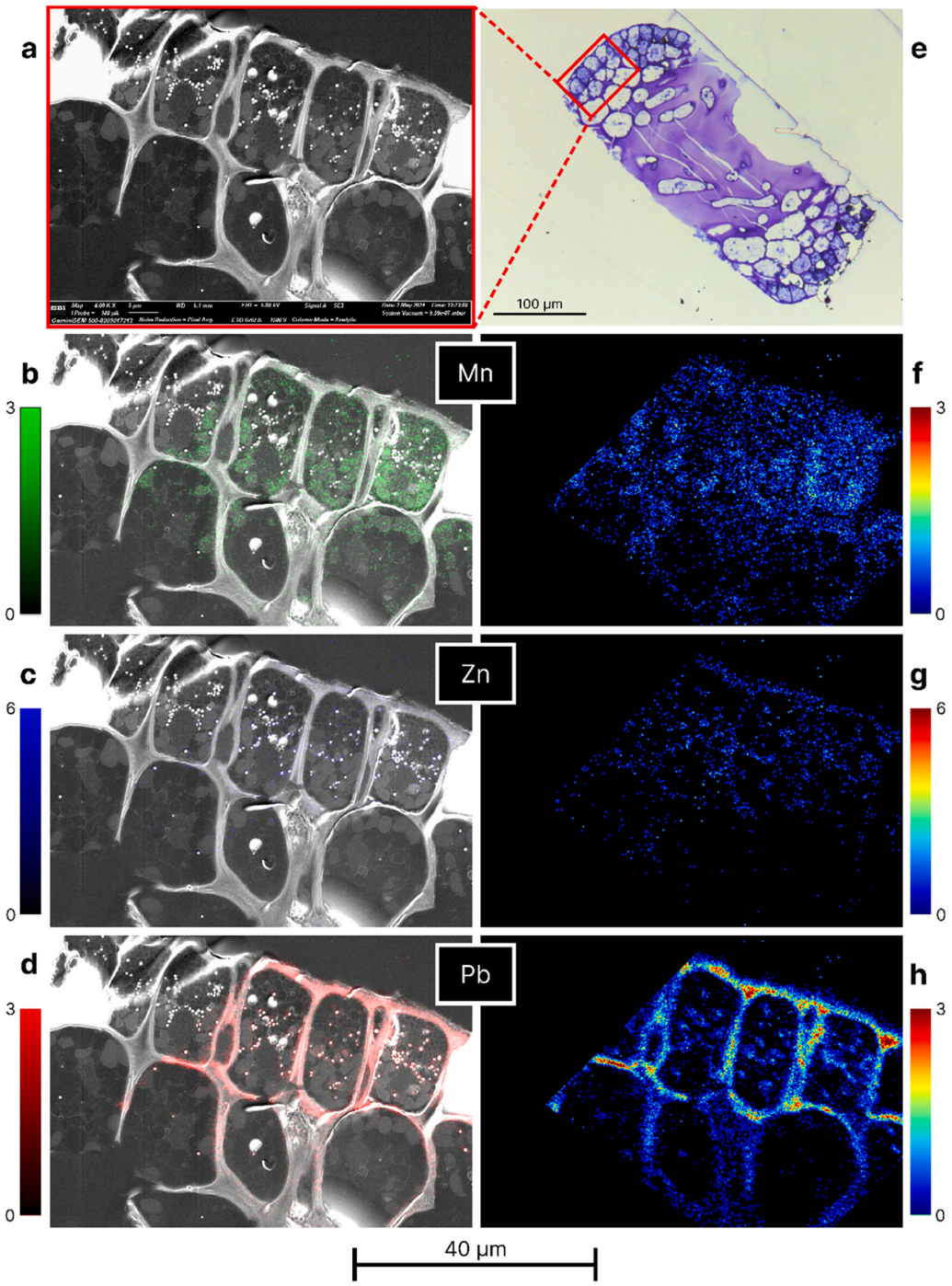

Fig. 2. SEM and NanoSIMS images of the P-P sample. a: SEM image. b-d: Elemental distribution maps of Mn, Zn, and Pb overlayed over the SEM image. e: Optical image of a section from a different *F. vesiculosus* sample stained with toluidine blue. f-h: Distribution maps with a color scale over for enhanced contrast. Color scale units are NanoSIMS read counts. Bottom scale applies to SEM and NanoSIMS images.

polluted site (U-P) than after being re-exposed at the unpolluted one (U-U). Conversely, Pb concentrations decreased in samples collected from the polluted site (P) and transported to the unpolluted site (P-U) compared to those re-exposed at the polluted site (P-P).

To ensure that this effect was not caused by differences during NanoSIMS analysis, we compared the variance between different analysis of the same sample and analyses of different samples (Fig. S5 of the supplementary material). The variance across samples was considerably higher, indicating that the observed differences were not caused by analytical artifacts.

We also compared the total concentrations of each element determined with ICP-MS across samples (Fig. 4), which displayed a completely different pattern from those measured with NanoSIMS. In this case, concentrations depended on the exposure site rather than whether the samples were autotransplants or cross-transplants. Transplants exposed at the polluted site had lower Mn and higher concentrations of other elements compared to those from the same origin exposed at the unpolluted site.

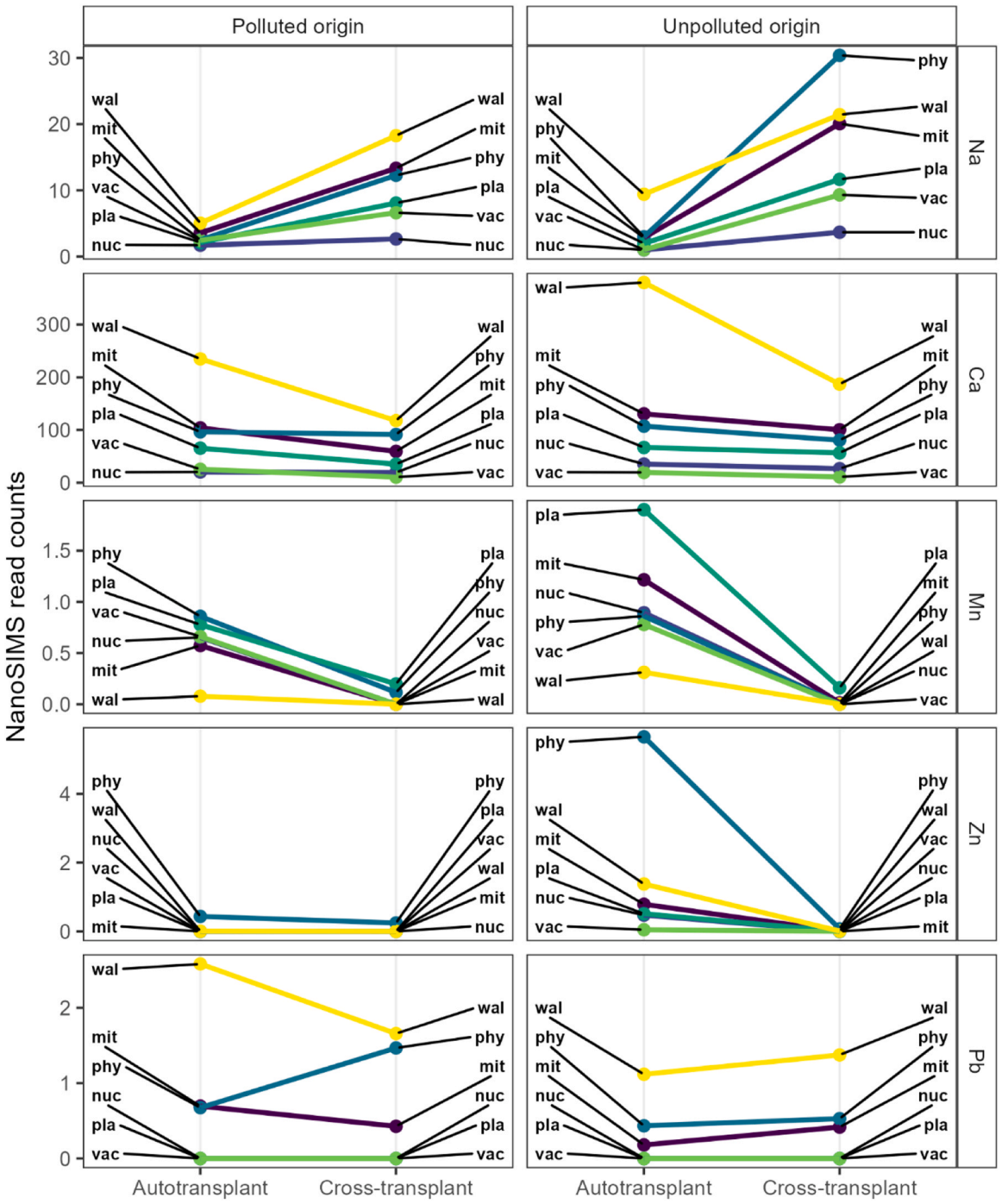

Fig. 3. Median intensity values obtained with NanoSIMS. Each column represents the collection site, and each line the intensity difference depending on the exposure site for each structure. Subcellular structures: wal: cell wall and extracellular polysaccharides; vac: vacuoles; pla: plastids; phy: physodes; nuc: nuclei; mit: mitochondria.

4. Discussion

4.1. Elemental distributions

Despite its relevance as an environmental pollutant, the localization of Pb within seaweeds was previously unknown. This study reveals that Pb is predominantly accumulated outside the cells, with only a minimal fraction being internalized. These findings align with previous results suggesting that seaweeds prevent the internalization of PTEs with limited metabolic functions [35]. The binding of Pb to the cell wall corroborates studies indicating that brown seaweeds use cell wall polysaccharides as a defense mechanism against Pb and Cd pollution [1]. The ability of seaweeds to prevent the internalization of these elements might explain why PTEs with lower toxicity to humans such as Cu are more toxic to algae than Cd and Pb [2,6].

The distribution of other elements (Ca, Mn, and Zn) matched the patterns observed through S-XRF analysis [35]. The highest concentrations of Ca were found in the cell walls, where it plays an important structural role [30]. However, as an essential nutrient, its concentrations were also high in mitochondria, plastids, and physodes compared to vacuoles. Mn, while an important nutrient for seaweeds due to its role in photosystem II, can also exert toxic effects on brown seaweeds [5]. Its

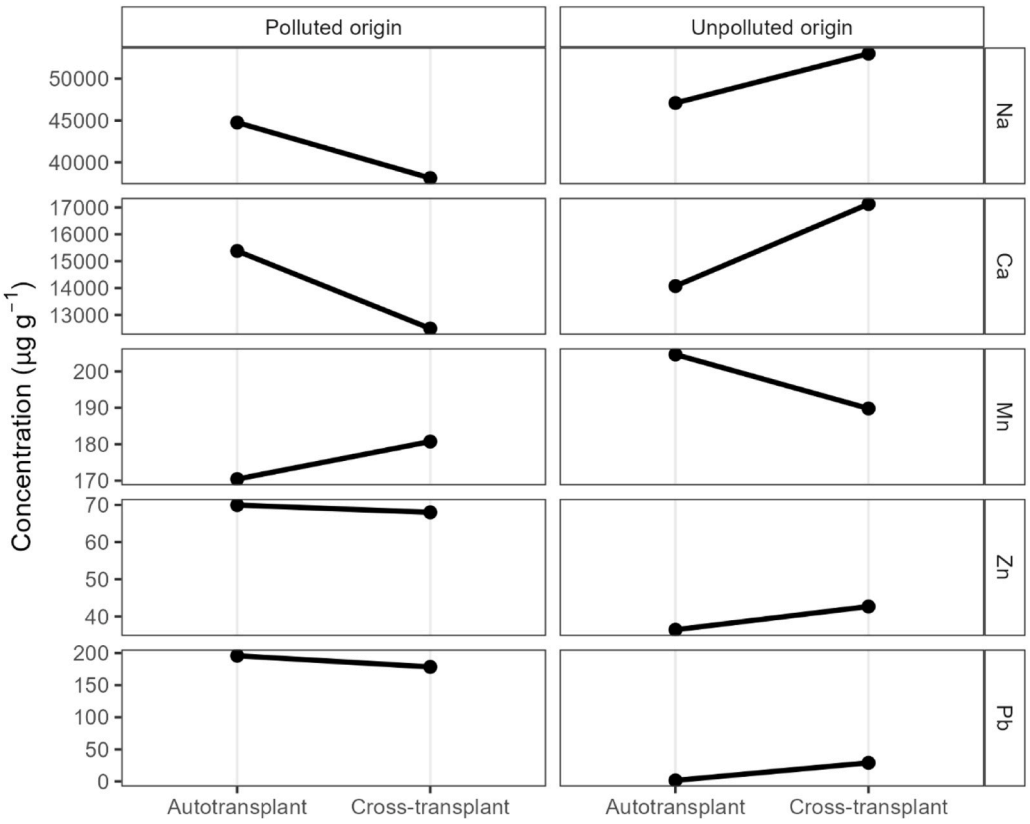

Fig. 4. Total elemental concentrations in each sample. Each column represents the collection site, and each line the concentration difference depending on the exposure site.

biological function explains its elevated concentrations inside plastids. High Mn concentrations were also found in physodes, possibly due to the affinity of these organelles for metallic cations. Since physodes act as storage sites for elements that have both toxic effects and metabolic functions, such as Co, Ni, Cu and Zn [35], this may also be the case for Mn. Zn, another essential PTE regulated through confinement in physodes, was strongly associated to these organelles, although some samples also displayed high Zn concentrations in the cell walls, a pattern consistent with previous observations [35].

Aside from Pb, Na was the only element in our study whose distribution in seaweeds had not yet been analyzed. Living in euhaline environments, seaweeds regulate Na primarily by preventing its internalization to maintain normal metabolic activity [32]. This is consistent with our results, which showed Na to be predominantly associated with the cell wall and physodes, the cellular structures involved in storing elements to mitigate toxicity. High Na concentrations were also detected in mitochondria, but this may be an artifact of the analysis. Structures with high concentrations of certain elements, such as Na in the cell wall and Zn in physodes, exhibit a halo of high concentrations around them. Because mitochondria are typically located near the cell wall, their apparent Na concentrations might be inflated by the halo effect. Larger and more widely distributed structures are less affected by this bias, but mitochondria concentrations for elements with high cell wall concentrations should be interpreted with caution.

4.2. Comparison across transplants

The transplantation experiment was designed to study the effect of exposure to different PTE concentrations, aiming to provide insights into the uptake mechanisms and dynamics. However, this analysis posed two main challenges, the first being data comparability.

Despite using identical sample preparation and analysis protocols, matrix effects—such as sample charge and surface topology—can influence ion yield and potentially introduce systematic differences [22]. To rule out such artifacts, we considered the element-specific patterns observed: if conductivity or other matrix-related factors were responsible, all elements in a sample would be similarly affected. Instead, different samples had the highest concentrations for different elements, which is inconsistent with a global matrix effect. Furthermore, while variations in pre-sputtering among analyzed regions could also affect the results, intra-sample variability was much lower than inter-sample variability, suggesting that the observed patterns reflect true biological differences rather than analytical artifacts. This was further supported by the consistency across the five consecutive analyses in each region, which showed nearly no variability. We are therefore reasonably confident in the comparability of the data.

Although autotransplants and cross-transplants were handled identically to account for the transportation and transplant preparation effects, autotransplants remained in their acclimated environmental conditions, whereas cross-transplants were exposed to new conditions. Changes in environmental physicochemical conditions can induce stress in seaweeds [14], potentially influencing membrane permeability, as observed in higher plants [8]. Therefore, we propose that the concentrations of most elements in both cross-transplants experienced similar changes due to the stress caused by different environmental conditions, although more direct metabolic studies would be needed to confirm this hypothesis.

This pattern contrasts with those observed for absolute concentrations in this (Fig. 3) and previous studies [36], where transplants moved to more polluted sites showed increased PTE concentrations, while those moved to less polluted sites exhibited decreases. The only element with lower total concentrations in the polluted site was Mn, which aligns with reports of high Mn at the unpolluted site [34]. The inconsistency between the effect of exposure at a different site on total and subcellular

concentrations fits previous S-XRF results [35], which showed no correlation with total concentrations. This discrepancy is likely caused by the presence of mineral particles on the seaweeds' surface, which often contain elemental concentrations significantly higher than those within seaweeds, and can represent a large fraction of the PTEs detected on total concentration analyses [33].

However, NanoSIMS sample preparation, particularly sectioning, may remove larger particles, especially those exceeding the section thickness. Therefore, NanoSIMS analyses only reflect PTEs located intracellularly or chemically bound to the cell wall, excluding one of the major sources of PTEs detected by ICP-MS. These differences explain the different patterns across samples, as changes in particle content would only affect ICP-MS results, whereas changes in intracellular PTEs detected by NanoSIMS may be overshadowed in total concentration analyses. As PTEs in mineral particles have low bioavailability, total concentrations do not reflect bioavailable concentrations, but NanoSIMS results would also be a poor proxy for metabolically regulated elements.

The disconnection between total and ultrastructural PTE concentrations also explains another unexpected pattern in our data. The polluted site was selected for its extreme Pb levels, previously detected in the sediment and seaweeds [33]. ICP-MS analysis confirmed this pollution, showing much higher Pb concentrations in samples from the polluted site compared to those from the unpolluted site, and increased Pb concentrations in response to exposure at the polluted site. However, while the total Pb concentrations at the polluted site were orders of magnitude higher than in U-U samples, differences detected with NanoSIMS were far smaller. This supports the hypothesis that the increase in total Pb concentrations is primarily due to surface-bound mineral particles, where contamination stems from a porcelain factory that ceased operation over 20 years ago. As a result, most Pb currently at the site is likely associated with mineral particles.

Pb was the only element for which the direction of cross-transplantation effects on the ultrastructural concentrations aligned with the pattern observed for total concentrations. This may be due to its lack of metabolic regulation: Pb is located almost exclusively extracellularly, whereas the other elements serve metabolic functions that require internalization and possible excretion. Stress caused by environmental changes is unlikely to affect Pb capture, which is governed by chemical binding, but may influence the intracellular concentrations of metabolically regulated elements. In both groups, the accumulation is at least partially reversible, as their concentrations decreased in the cross-transplants. This reversibility was evident across different intracellular organelles, suggesting a continuous flux of these elements. In physodes, this discharge may involve exchange with the cytoplasm, but physodes can also fuse with the cell membrane releasing their contents into the apoplast [29], which could serve as an alternative pathway for PTE expulsion.

5. Conclusions

Our results indicate that Pb, due to its toxicity and lack of biological function, is excluded from cells and retained in the cell wall. In contrast, PTEs with intracellular functions such as Mn and Zn are internalized and sequestered into physodes. Consequently, Pb concentrations in seaweed cells are governed by equilibrium between environmental bioavailable concentrations and cell wall binding sites, whereas essential PTEs do not respond directly to changes in environmental concentrations, likely being controlled by metabolic regulation. This distinction has important implications for seaweed conservation, as high environmental concentrations of extracellular PTE like Pb might have less of an impact on seaweed populations, whereas metabolic PTEs may pose greater toxicity. Still, high total concentrations of metabolic PTEs in seaweeds might be safe if they are attached to mineral particles, as these do not directly reflect intracellular levels. Thus, both the composition and bioavailability of elemental pollution are essential for understanding its impact on seaweeds.

Environmental implication

This study provides insight into how seaweeds interact with potentially toxic elements (PTEs), helping us understand the impacts of metal pollution on seaweed health, population dynamics, and the ecosystems they support. It demonstrates that the internalization of PTEs depends on their metabolic function, with essential PTEs such as Zn and Mn being actively taken up and regulated metabolically, whereas non-essential PTEs like Pb are excluded and bound to the cell wall. This distinction helps explain why seaweeds are more resistant to pollution by certain PTEs.

CRediT authorship contribution statement

Jesús R. Aboal: Writing – review & editing, Investigation, Funding acquisition, Conceptualization. **Yosuke Yamada:** Writing – review & editing, Supervision, Investigation. **Conxi Rodríguez-Prieto:** Writing – review & editing. **J. Ángel Fernández:** Writing – review & editing, Investigation, Funding acquisition. **Motoo Ito:** Writing – review & editing, Supervision, Methodology, Investigation, Funding acquisition. **Antón Vázquez-Arias:** Writing – original draft, Visualization, Investigation, Formal analysis, Data curation, Conceptualization.

Declaration of Generative AI and AI-assisted technologies in the writing process

During the preparation of this work the authors used ChatGPT for assistance with refining language and improving the clarity of the manuscript. After using this tool, the authors reviewed and edited the content as needed and take full responsibility for the content of the publication.

Declaration of Competing Interest

The authors declare that they have no known competing financial interests or personal relationships that could have appeared to influence the work reported in this paper.

Acknowledgements

This research has received funding from the Spanish Ministry of Science, Innovation and Universities (MCIN/AEI), through the "Proyectos de Generación del Conocimiento 2022" program under the project ID "PID2022–142802NB-I00, CoastProtect". Antón Vázquez-Arias is grateful to the Spanish Ministerio de Ciencia, Innovación y Universidades for a grant awarded within the Programa de Formación de Profesorado Universitario (grant number FPU19/01989). Yosuke Yamada is grateful to JSPS for a KAKENHI grant (grant number JP24K21331), to JST for a grant awarded within the FOREST program (grant number JPMJFR2070), and to MEXT for support within the World Premier International Research Center Initiative (WPI). Motoo Ito is grateful to JSPS for a KAKENHI grant (grant number JP23H01238).

We want to thank the Cryoelectron Microscopy Laboratory of the Centro Nacional de Biotechnology (CNB-CSIC) for performing high pressure freezing to the samples, and the Electron Microscopy Laboratory for their help in the steps of cryosubstitution, embedding, and microscopy work. We also want to thank RIAIDT-USC for the use of their analytical facilities. Finally, we want to thank Dr. Atsuko Kobayashi from Kochi University for her assistance with ultramicrotome sectioning.

Appendix A. Supporting information

Supplementary data associated with this article can be found in the online version at doi:10.1016/j.jhazmat.2025.139646.

Data availability

Data will be made available on request.

References

[1] Andrade, L.R., Leal, R.N., Noseda, M., Duarte, M.E.R., Pereira, M.S., Mourão, P.A. S., et al., 2010. Brown algae overproduce cell wall polysaccharides as a protection mechanism against the heavy metal toxicity. Mar Pollut Bull 60, 1482–1488. https://doi.org/10.1016/j.marpolbul.2010.05.004.

[2] Babu, M.Y., Palanikumar, L., Nagarani, N., Devi, V.J., Kumar, S.R., Ramakritinan, C.M., et al., 2014. Cadmium and copper toxicity in three marine macroalgae: evaluation of the biochemical responses and DNA damage. Environ Sci Pollut Res 21, 9604–9616. https://doi.org/10.1007/s11356-014-2999-0.

[3] Castillo, A., Valdés, J., Marambio, Y., Figueroa, L., Letelier, J., Carcamo, F., 2023. Metal(loid)s content in Concholepas concholepas (Mollusca) and human health assessment in a coastal environmental sacrifice zone, central Chile (~32°S). Mar Pollut Bull 197, 115738. https://doi.org/10.1016/j.marpolbul.2023.115738.

[4] Cima, F., Varello, R., 2022. Potential disruptive effects of copper-based antifouling paints on the biodiversity of coastal macrofouling communities. Environ Sci Pollut Res 30, 8633–8646. https://doi.org/10.1007/s11356-021-17940-2.

[5] Costa, G.B., Simioni, C., Ramlov, F., Maraschin, M., Chow, F., Bouzon, Z.L., et al., 2017. Effects of manganese on the physiology and ultrastructure of *Sargassum cymosum*. Environ Exp Bot 133, 24–34. https://doi.org/10.1016/j.envexpbot.2016.09.007.

[6] Debelius, B., Forja, J.M., DelValls, Á., Lubián, L.M., 2009. Toxicity and bioaccumulation of copper and lead in five marine microalgae. Ecotoxicol Environ Saf 72, 1503–1513. https://doi.org/10.1016/j.ecoenv.2009.04.006.

[7] Decelle, J., Veronesi, G., Gallet, B., Stryhanyuk, H., Benettoni, P., Schmidt, M., et al., 2020. Subcellular chemical imaging: new avenues in cell biology. Trends Cell Biol 30 (3), 173–188. https://doi.org/10.1016/j.tcb.2019.12.007.

[8] Demidchik, V., Straltsova, D., Medvedev, S.S., Pozhvanov, G.A., Sokolik, A., Yurin, V., 2014. Stress-induced electrolyte leakage: the role of K^+-permeable channels and involvement in programmed cell death and metabolic adjustment. J Exp Bot 65 (5), 1259–1270. https://doi.org/10.1093/jxb/eru004.

[9] Dolbeth, M., Arenas, F., 2021. Marine ecosystems: types. Their Importance and Main Impacts. Springer, Cham, pp. 1–17. https://doi.org/10.1007/978-3-319-71064-8_38-1.

[10] Ender, E., Subirana, M.A., Raab, A., Krupp, E.M., Schaumlöffel, D., Feldmann, J., 2019. Why is NanoSIMS elemental imaging of arsenic in seaweed (*laminaria digitata*) important for understanding of arsenic biochemistry in addition to speciation information? J Anal Spectrom 34, 2295–2302. https://doi.org/10.1039/c9ja00187e.

[11] Gamo, T., 2020. Anthropogenic Lead Pollution in the Ocean. Springer, Singapore, pp. 295–306. https://doi.org/10.1007/978-981-32-9224-6_21.

[12] García-Seoane, R., Aboal, J.R., Boquete, M.T., Fernández, J.Á., 2018. Biomonitoring coastal environments with transplanted macroalgae: a methodological review. Mar Pollut Bull 135, 988–999. https://doi.org/10.1016/j.marpolbul.2018.08.027.

[13] García-Seoane, R., Fernández, J.Á., Villares, R., Aboal, J.R., 2018. Use of macroalgae to biomonitor pollutants in coastal waters: optimization of the methodology. Ecol Indic 84, 710–726. https://doi.org/10.1016/j.ecolind.2017.09.015.

[14] Hurd, C.L., Harrison, P.J., Bischof, K., Lobban, C.S., 2014. Seaweed Ecology and Physiology. Cambridge University Press, pp. 294–348. https://doi.org/10.1017/cbo9781139192637.008. Physico-chemical factors as environmental stressors in seaweed biology.

[15] Ito, M., Tomioka, N., Uesugi, M., Yamaguchi, A., Shirai, N., Ohigashi, T., et al., 2022. A pristine record of outer Solar System materials from asteroid Ryugu's returned sample. Nat Astron 6, 1163–1171. https://doi.org/10.1038/s41550-022-01745-5.

[16] Lagerström, M., Ferreira, J., Ytreberg, E., Eriksson-Wiklund, A.K., 2020. Flawed risk assessment of antifouling paints leads to exceedance of guideline values in baltic sea marinas. Environ Sci Pollut Res 27, 27674–27687. https://doi.org/10.1007/s11356-020-08973-0.

[17] Lebeau, D., Leroy, N., Doizi, D., Wu, T.-D., Guerquin-Kern, J.L., Perrin, L., et al., 2021. Mass spectrometry – based imaging techniques for iodine-127 and iodine-129 detection and localization in the brown alga *Laminaria digitata*. J Environ Radio 231, 106552. https://doi.org/10.1016/J.JENVRAD.2021.106552.

[18] Levings, C.D., Barry, K.L., Grout, J.A., Piercey, G.E., Marsden, A.D., Coombs, A.P., et al., 2004. Effects of acid mine drainage on the estuarine food web, britannia beach, howe sound, British Columbia, Canada. Hydrobiologia 525, 185–202. https://doi.org/10.1023/B:HYDR.0000038866.20304.3d.

[19] Moore, K.L., Lombi, E., Zhao, F.J., Grovenor, C.R.M., 2012. Elemental imaging at the nanoscale: NanoSIMS and complementary techniques for element localisation in plants. Anal Bioanal Chem 402, 3263–3273. https://doi.org/10.1007/s00216-011-5484-3.

[20] Nieto, J.M., Sarmiento, A.M., Olías, M., Canovas, C.R., Riba, I., Kalman, J., et al., 2007. Acid mine drainage pollution in the tinto and odiel rivers (Iberian Pyrite Belt, SW Spain) and bioavailability of the transported metals to the huelva estuary. Environ Int 33, 445–455. https://doi.org/10.1016/j.envint.2006.11.010.

[21] Nunes, M., Leston, S., 2022. Springer, Cham, pp. 155–166. https://doi.org/10.1007/978-3-319-98536-7_9. Coastal Pollution: An Overview.

[22] Nuñez, J., Renslow, R., Cliff, J.B., Anderton, C.R., 2018. NanoSIMS for biological applications: current practices and analyses. Biointerphases 13, 03B301. https://doi.org/10.1116/1.4993628.

[23] Outridge, P.M., Hobson, K.A., McNeely, R., Dyke, A., 2002. A comparison of modern and preindustrial levels of Mercury in the teeth of beluga in the Mackenzie delta, northwest territories, and Walrus at Igloolik, Nunavut, Canada. Arctic 55, 123–132. https://doi.org/10.14430/arctic696.

[24] Pessarrodona, A., Assis, J., Filbee-Dexter, K., Burrows, M.T., Gattuso, J.P., Duarte, C.M., et al., 2022. Global seaweed productivity. Sci Adv 8. https://doi.org/10.1126/sciadv.abn2465.

[25] Poczatek, C., Kaufman, Z., Lechene, C., 2012. Open Image Plugin Guide Open MIMS Images 118.

[26] R. Core Team, 2024. R: A Language and Environment for Statistical Computing.

[27] Sack, H., 2023. The importance of coastal and marine ecosystems, in: a regional assessment of marine and coastal EbA in SADC. South Afr Inst Int Aff 16–20.

[28] Schindelin, J., Arganda-Carreras, I., Frise, E., Kaynig, V., Longair, M., Pietzsch, T., et al., 2012. Fiji: an open-source platform for biological-image analysis. Nat Methods 9, 676–682. https://doi.org/10.1038/nmeth.2019.

[29] Schoenwaelder, M.E.A., 2002. The occurrence and cellular significance of physodes in brown algae. Phycologia 41, 125–139. https://doi.org/10.2216/i0031-8884-41-2-125.1.

[30] Terauchi, M., Nagasato, C., Inoue, A., Ito, T., Motomura, T., 2016. Distribution of alginate and cellulose and regulatory role of calcium in the cell wall of the brown alga *Ectocarpus siliculosus* (Ectocarpales, Phaeophyceae). Planta 244, 361–377. https://doi.org/10.1007/s00425-016-2516-4.

[31] Umanzor, S., Ladah, L., Calderon-Aguilera, L.E., Zertuche-González, J.A., 2019. Testing the relative importance of intertidal seaweeds as ecosystem engineers across tidal heights. J Exp Mar Biol Ecol 511, 100–107. https://doi.org/10.1016/j.jembe.2018.11.008.

[32] Van Ginneken, V., 2018. Some mechanism seaweeds employ to cope with salinity stress in the harsh euhaline oceanic environment. Am J Plant Sci 09, 1191–1211. https://doi.org/10.4236/ajps.2018.96089.

[33] Vázquez-Arias, A., Aboal, J.R., Fernández, J.Á., 2023. What dead seaweeds can tell us about metal uptake and their application to control marine pollution. J Hazard Mater 459, 132216. https://doi.org/10.1016/j.jhazmat.2023.132216.

[34] Vázquez-Arias, A., Boquete, M.T., Fernández, J.Á., Aboal, J.R., 2025. Assessing the effectiveness of seaweed transplants in reflecting seawater pollution levels. Environ Pollut 377, 126456. https://doi.org/10.1016/J.ENVPOL.2025.126456.

[35] Vázquez-Arias, A., Boquete, M.T., Martín-Jouve, B., Tucoulou, R., Rodríguez-Prieto, C., Fernández, J.Á., et al., 2024. Nanoscale distribution of potentially toxic elements in seaweeds revealed by synchrotron X-ray fluorescence. J Hazard Mater 480, 136454. https://doi.org/10.1016/j.jhazmat.2024.136454.

[36] Vázquez-Arias, A., Pacín, C., Ares, Á., Fernández, J.Á., Aboal, J.R., 2023. Do we know the cellular location of heavy metals in seaweed? An up-to-date review of the techniques. Sci Total Environ 856, 159215. https://doi.org/10.1016/j.scitotenv.2022.159215.

[37] Verhaeghe, E.F., Fraysse, A., Guerquin-Kern, J.L., Wu, T.-D., Devès, G., Mioskowski, C., et al., 2008. Microchemical imaging of iodine distribution in the brown alga *Laminaria digitata* suggests a new mechanism for its accumulation. J Biol Inorg Chem 13, 257–269. https://doi.org/10.1007/s00775-007-0319-6.

[38] Wickham, H., 2016. ggplot2: Elegant Graphics for Data Analysis. Springer-Verlag New York.

[39] Witt, B., Schaumlöffel, D., Schwerdtle, T., 2020. Subcellular localization of copper—cellular bioimaging with focus on neurological disorders. Int J Mol Sci. https://doi.org/10.3390/ijms21072341.

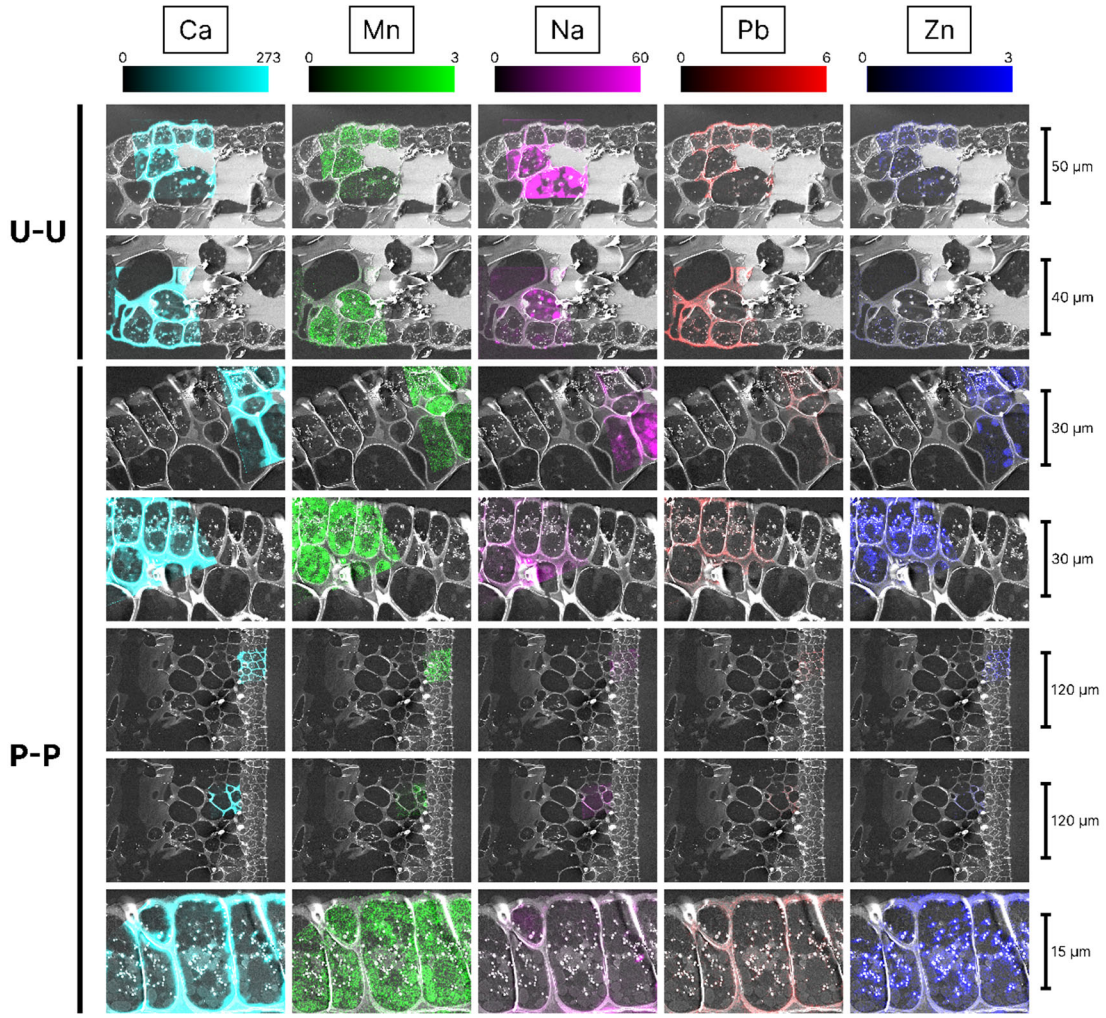

Figure S1. Elemental distribution maps of different regions of the samples U-U and P-P obtained with NanoSIMS, overlayed over SEM images of the same region. Color scale units are NanoSIMS read counts.

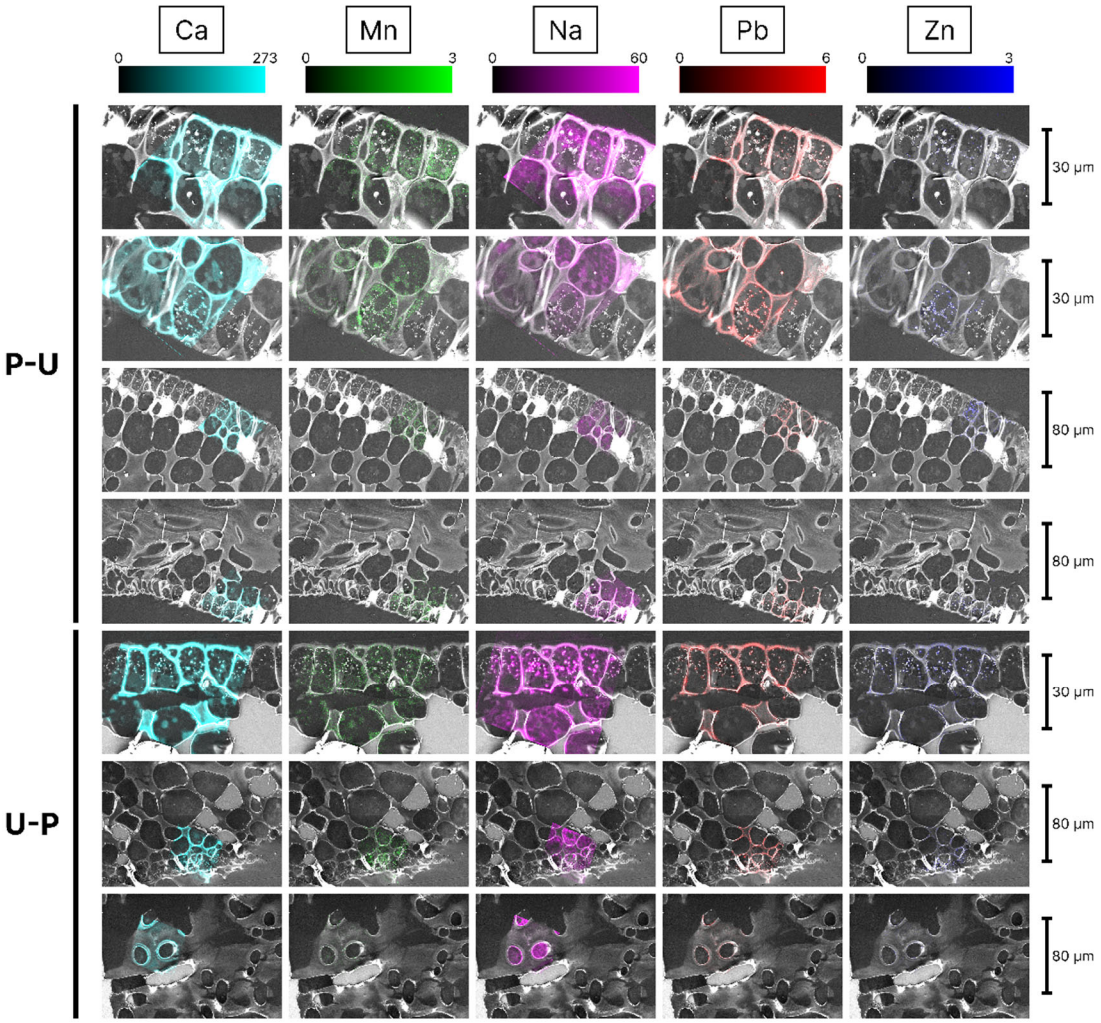

Figure S2. Elemental distribution maps of different regions of the samples P-U and U-P obtained with NanoSIMS, overlayed over SEM images of the same region. Color scale units are NanoSIMS read counts.

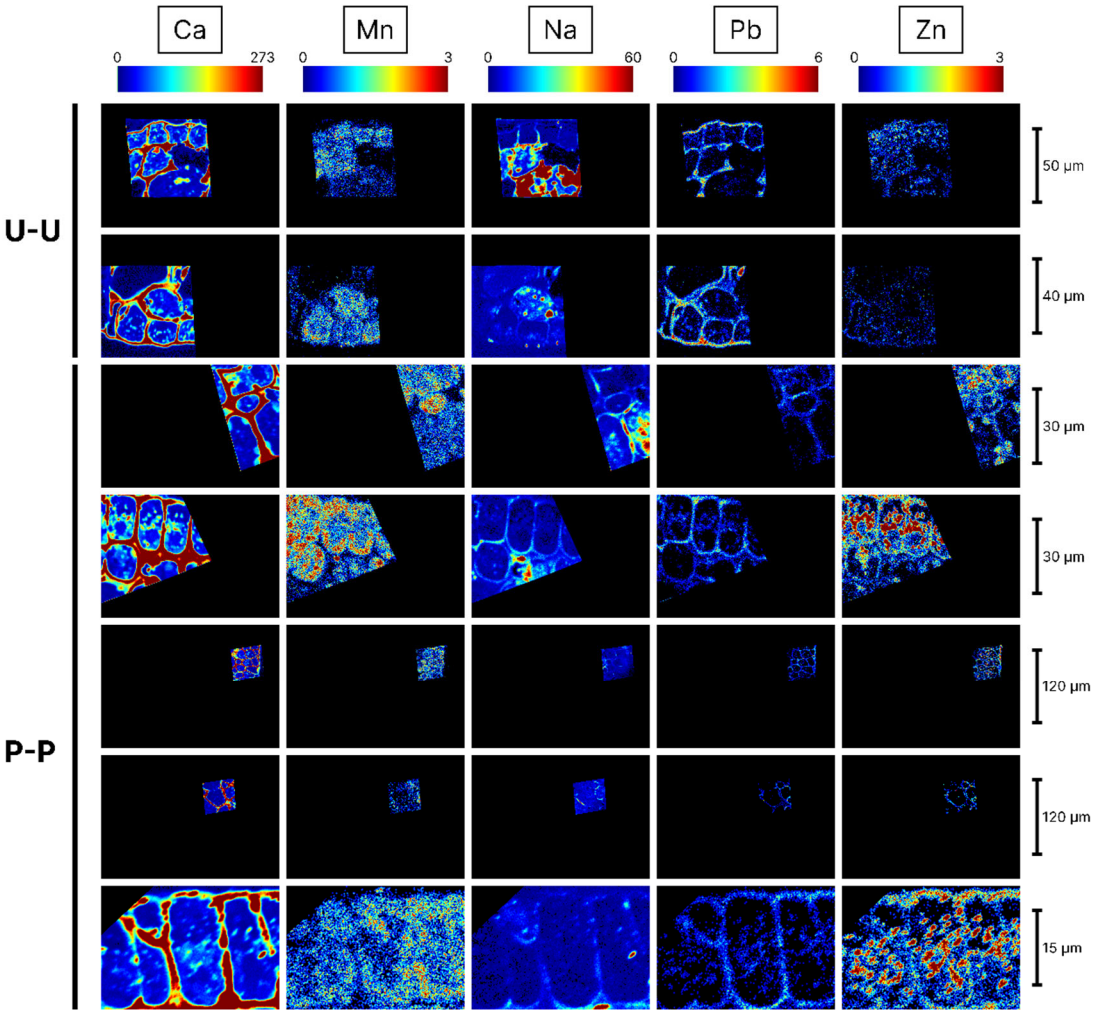

Figure S3. Elemental distribution maps of different regions of the samples U-U and P-P obtained with NanoSIMS. Color scale units are NanoSIMS read counts.

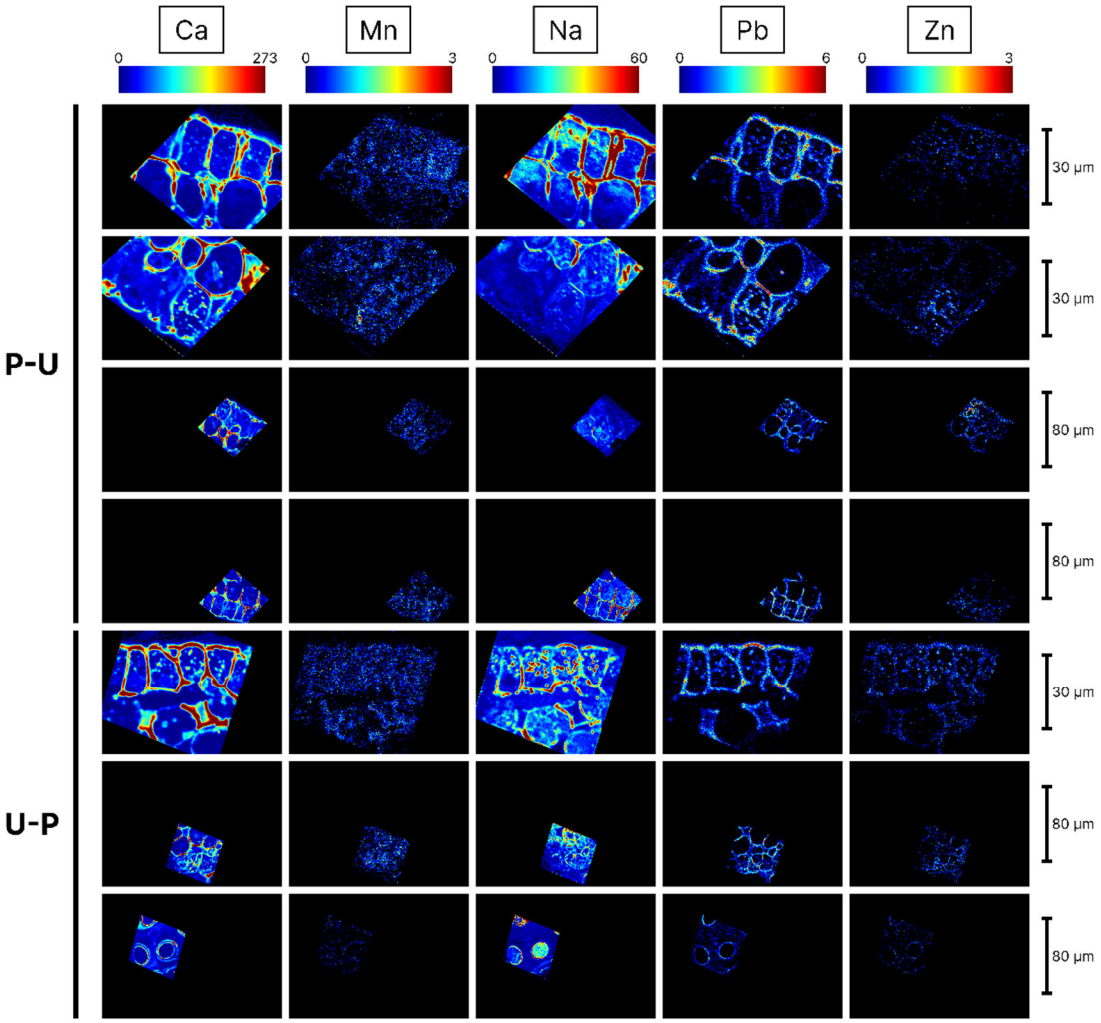

Figure S4. Elemental distribution maps of different regions of the samples P-U and U-P obtained with NanoSIMS. Color scale units are NanoSIMS read counts.

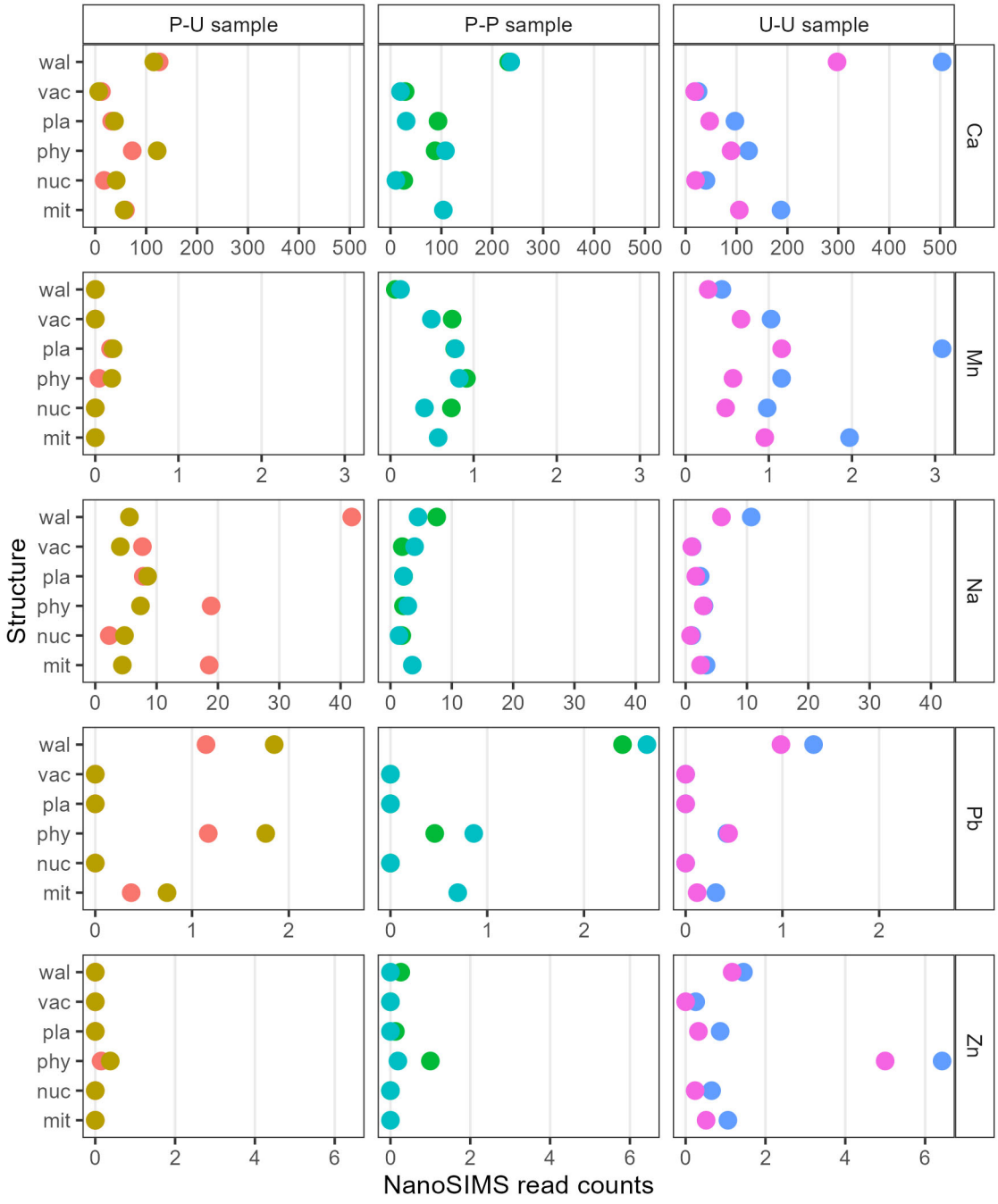

18

19 **Figure S5**. Median intensity values obtained with NanoSIMS for the different subcellular
20 structures in each sample and subregion. Each column represents a different sample,
21 and each color in each column corresponds to a different region within that sample.
22 Subcellular structures: nuc: nuclei; phy: physodes; pla: plastids; mit: mitochondria; vac:
23 vacuoles; wal: cell wall and extracellular polysaccharides.

24

25